Nonlinear Dyn (2025) 113:21951–21969
https://doi.org/10.1007/s11071-025-11283-0

RESEARCH

Extreme multistability and complex bifurcation routes in a memristive Hopfield neural network

Jiakai Lu · Fuhong Min · Linghu Gan · Wei Zhu

Received: 28 February 2025 / Accepted: 19 April 2025 / Published online: 19 May 2025
© The Author(s), under exclusive licence to Springer Nature B.V. 2025

Abstract Neural networks exhibit complex dynamical behaviors, encompassing multistability, neural firing patterns, and bifurcation phenomena. Investigating extreme multistability is crucial for advancing our understanding of the human brain and its associated disorders. To elucidate the underlying mechanisms and develop effective control strategies for neural models, this study employs a non-autonomous memristive Hopfield neural network (MHNN) with two neurons. The proposed model effectively demonstrates multistability and the coexistence of diverse spiking behaviors. To provide deeper insights into these phenomena, an innovative analytical approach is adopted, complemented by numerical validation. A discrete mapping structure is formulated, and the line equilibrium points of the proposed model are systematically analyzed. The coexistence of bifurcation behaviors is explored through numerical bifurcation diagrams and a semi-analytical bifurcation tree. Furthermore, the presence of infinitely many coexisting attractors and unstable periodic orbits within chaotic regions is revealed through initial condition bifurcation and local attraction basin analysis. The system exhibits a wide range of firing dynamics, including stable spiking patterns and transitions from unstable to stable firing states, as demonstrated through time series analysis. To achieve enhanced control over the system's dynamics, a rotational control strategy is introduced, facilitating the generation of an infinite number of coexisting attractors in any direction within the two-dimensional space. Finally, the theoretical findings are substantiated through the empirical observation of coexisting periodic orbits using a Field-Programmable Gate Array (FPGA).

Keywords Memristive Hopfield neural network · Extreme multistability · Unstable periodic orbits · Rotation control

1 Introduction

Neurons, as the fundamental building blocks of biological brains, exhibit highly complex and nonlinear behaviors. To advance the understanding and modeling of the brain, artificial neural networks (ANNs) have been developed to abstract key aspects of biological information processing [1–3]. Among these, the Hopfield Neural Network (HNN), originally introduced in 1984 [4], serves as a bridge between neural dynamics and electronic circuits, rendering it particularly suitable for both theoretical analysis and hardware implementation. Due to its distinctive network architecture, HNN can generate a diverse range of complex dynamical behaviors, including periodic, quasi-periodic, and chaotic dynamics [5–7]. These

J. Lu · F. Min (✉) · L. Gan · W. Zhu
School of Electrical and Automation Engineering, Nanjing Normal University, Nanjing 210023, China
e-mail: minfuhong@njnu.edu.cn

properties establish HNN as a crucial tool for exploring the computational mechanisms underlying neural activity.

To further enrich the dynamical phenomena, the memristor [8], recognized as the fourth fundamental circuit element, has been incorporated into the design of HNNs. As a novel two-terminal device, the memristor's inherent plasticity and nonvolatility are closely associated with the memory properties of neurons [9]. These characteristics make the memristor an ideal component for constructing biologically inspired neural models. Recent studies have demonstrated that memristive Hopfield Neural Networks (MHNNs) can exhibit a broader spectrum of dynamical behaviors, i.e., multistability [10, 11]. The multistable behavior exhibited by memristive neural networks has attracted considerable research interest in recent years, as it reflects the diversity and complexity of the brain's nervous system [12, 13]. For instance, the variations with initial conditions lead to four coexisting attractors in a three-neuron-based MHNN [14]. Moreover, the coexistence of limit cycles with different period, fixed point or strange attritor, were always observed in a time-delay MHNNs [15]. Overall, MHNNs demonstrate behaviors such as multistability and bifurcations, which are crucial for understanding neural dynamics, and thereby have significant applications in pattern recognition [16], secure communication [17, 18], signal detection [19, 20], and the analysis of natural phenomena [21, 22]. Although many studies have examined these dynamic characteristics [23], the phenomenon of extreme multistability characterized by the presence of an infinite number of coexisting attractors, remains insufficiently investigated. While parameter tuning is often employed to guide systems toward multiple attractors [24, 25], the precise control over attractor positions within the phase space remains a significant challenge [26–28].

To address the above-mentioned problem, researchers have proposed several attractor control methods, including offset control and rotation control. For instance, the attractor positions are able to be determined by initial conditions, leading the coexisting attractors to spatial shift along a specific trajectory with identical shapes but different locations [29, 30]. In addition, a rotation-based approach grounded in Euler's rotation theorem has been employed to adjust attractor orientation while preserving their geometric features [31]. However, the broader capability to position attractors flexibly throughout the phase space deserve further exploration, by combining multiple control methods.

Besides, MHNNs have demonstrated significant potential in elucidating complex neural dynamics, offering valuable insights into bifurcation structures and attractor behaviors. One effective approach to further investigating these dynamics involves transforming the continuous system into a discrete map, which unveils intricate bifurcation patterns and unstable periodic orbits [32], thereby enabling a more precise analysis and a deeper understanding of the system's dynamical properties. Furthermore, bifurcation trees have been observed in Shinriki circuits, while pitchfork bifurcations have been identified in Tabu neurons [33, 34]. By integrating the discrete mapping technique with conventional dynamic analysis, researchers can attain a more comprehensive understanding of MHNNs, paving the way for further exploration of their complex behaviors.

Encouraged by above literatures, a two-neuron MHNN model with more efficient memristive synapses will be studied through the discrete mapping method, providing new insights into more flexible and robust neural network models. A comparison of the results with those of related previous studies is shown in Table 1, and the main contributions and novel aspects of this study are as follows: (1) A MHNN model with two neurons is proposed, demonstrating the capability of exhibiting extreme multistability. (2) A semi-analytical approach is employed to investigate the coexisting bifurcation routes and unstable orbits within the system. (3) Building upon the original model, a rotation matrix is incorporated to enhance its dynamical behavior, enabling the generation of an infinite number of attractors in any direction by adjusting the initial value and rotation angle.

The remainder of this paper is organized as follows: Sect. 2 outlines the construction and equilibrium analysis of the MHNN model, along with its discretization. Section 3 investigates the initial condition-dependent dynamics, including bifurcations and spiking patterns, while Sect. 4 introduces the application of rotation control. Section 5 demonstrates the coexisting behavior observed through FPGA implementation. Finally, Section 6 concludes the study.

Table 1 Comparison of different HNN models

References	Memristor	Representative dynamical behaviors	Coexisting types	Control strategy	Hardware implementation
[35]	hyperbolic-type memristor	coexistence, period, chaos, extreme multistability	infinitely many	–	–
[36]	–	chaos, period, quasi-period, limit cycle	3	–	Analog circuit
[37]	simplified voltage controlled memristor	chaos, period,	–	offset	Analog circuit
This article	A modified hyperbolic-type memristor	chaos, period, extreme multistability, unstable period orbit	infinitely many	rotation	Digital circuit

2 Memristive Hopfield neural network

Considering the 2D HNN described in Ref. [38], the governing equation of the system is given by

$$\dot{\mathbf{x}} = -\mathbf{x} + \mathbf{W}\tanh(\mathbf{x}) + \mathbf{I} \tag{1}$$

where $\mathbf{x} = [x_1, x_2]^{\mathrm{T}}$ is the neuronal state vector, while the synaptic weight matrix $\mathbf{W} = (w_{ij})$ represents the connection strengths between neurons i and j. The bias current vector is given by $\mathbf{I}^T = [I_1, I_2]$, and $\tanh(\mathbf{x}) = [\tanh(x_1), \tanh(x_2)]^{\mathrm{T}}$ is the activation function.

The MHNN is constructed by substituting a resistive self-connection synaptic weight with a memristive one. The connection topology of the MHNN with two neurons is shown in Fig. 1. Consequently, the weight of the memristive autapse becomes variable. To achieve this, a novel hyperbolic-type memristor is selected as the candidate, and its mathematical model is defined as follows:

$$\begin{cases} i_M = W(\varphi)\tanh(v_M)v_M = \cos(\pi\varphi)\tanh(v_M)v_M \\ \dot{\varphi} = v_M \end{cases} \tag{2}$$

where v_M and i_M are the voltage and current, respectively. In terms of testing the characteristics of the memristor, here initial state $\varphi(0) = 0$ is set while applying an excitation signal $v = A\sin(2\pi Ft)$ to the memristor, where A and F are the amplitude and frequency of the stimulus, respectively. First, by keeping the amplitude constant and adjusting the frequency, three pinched hysteresis loops are shown in Fig. 2a. It is evident that all three hysteresis loops are pinched at the origin, with the region of the hysteresis loop gradually contracting as the signal frequency increases from 0.5 to 0.8 to 1.2. By holding the frequency while varying the amplitude A, three pinched hysteresis loops are observed, as depicted in Fig. 2b. At a specific amplitude $A = 2$, the hysteresis loop is only pinched at the origin (P_0). However, when the stimulus amplitude is increased at $A = 4$, the hysteresis loop exhibits pinch points at three locations (P_0, P_1, P_2), and further increasing the amplitude at $A = 9$, results in five pinch points (P_0, P_3, P_4, P_5, P_6). This memristor demonstrates multiple pinch points, in contrast to others that exhibit only a single pinch [39–41]. Thus, the complexity of this memristor is more than those with only one pinch point.

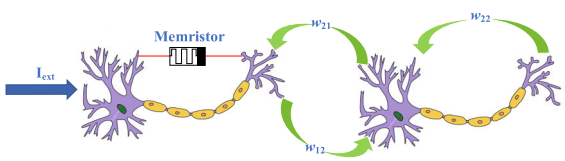

Fig. 1 Schematic diagram of memristive neuron coupling

With the previously mentioned memristor simulating the autapse of neuron 1, the mathematical model is expressed by

$$\begin{cases} \dot{x}_1 = -x_1 + kx_1\cos(\pi x_3)\tanh(x_1) + w_{21}\tanh(x_2) + I_{ext} \\ \dot{x}_2 = -x_2 + w_{12}\tanh(x_1) + w_{22}\tanh(x_2) \\ \dot{x}_3 = x_1 \end{cases} \tag{3}$$

where x_1, x_2 are the membrane potential of the two neurons, and x_3 is the internal variable of the memristor. k represents coupling strength between the neuron and memristor.w_{21}, w_{12} and w_{22} denotes the synaptic weights. $I_{ext} = I_m\sin(\omega t)$ is the external sinusoidal current applied to neuron 1 where I_m and ω stand for the amplitude and frequency, respectively.

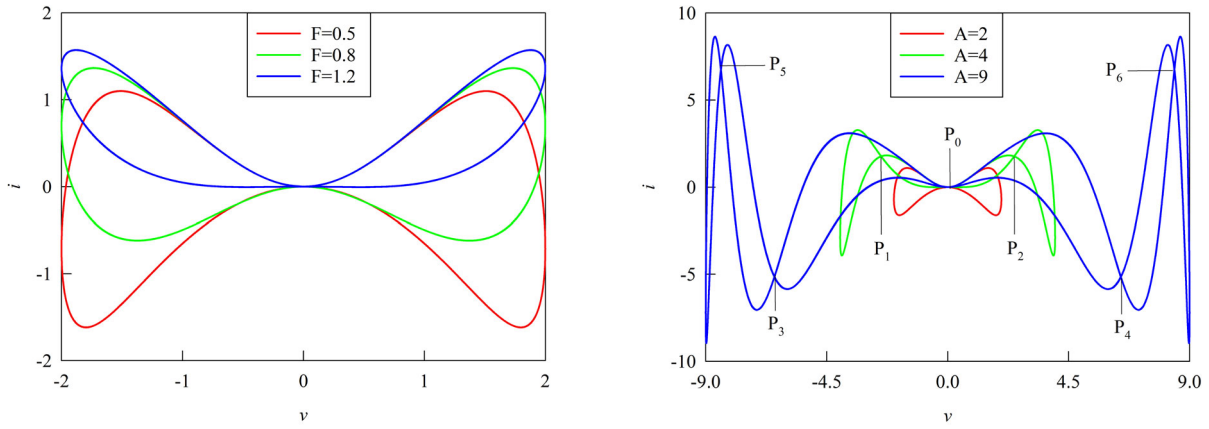

(a) (b)

Fig. 2 Three pinched hysteresis loops of local active memristor: **a** $A = 2$ with three values of stimulus frequency F, **b** $F = 0.5$ with three values of stimulus amplitude A

Hence, the MHNN is a nonautonomous dynamical model with three dimensions.

Let the left of Eq. (3) equal to zero, the equilibrium points expressed by $E_0 = (x_{1e}, x_{2e}, x_{3e})$ can be obtained by the following equations as

$$\begin{cases} 0 = -x_{1e} + kx_{1e}\cos(\pi x_{3e})\tanh(x_{1e}) + w_{21}\tanh(x_{2e}) + I_{ext} \\ 0 = -x_{2e} + w_{12}\tanh(x_{1e}) + w_{22}\tanh(x_{2e}) \\ 0 = x_{1e} \end{cases} \tag{4}$$

wherex_{2e} are the solutions of

$$x_{2e} = -\frac{w_{22}}{w_{21}} I_{ext} \tag{5}$$

Obviously, the system has a line of AC equilibrium points that expressed by

$$E_0 = \left(0, -\frac{w_{22}}{w_{21}} I_{ext}, x_{3e}\right), \tag{6}$$

where x_{3e} can be any value. The corresponding simplified Jacobian matrix of Eq. (3) is

$$\mathbf{J_0} = \begin{pmatrix} -1 & -w_{21}\mathrm{sech}^2 x_{2e} & 0 \\ -w_{12} & -w_{22}\mathrm{sech}^2 x_{2e} - 1 & 0 \\ 1 & 0 & 0 \end{pmatrix} \tag{7}$$

The characteristic equation from Eq. (6) is calculated as

$$\lambda^3 + p_1\lambda^2 + p_2\lambda + p_3 = 0, \tag{8}$$

where

$$\begin{cases} p_1 = 2 + w_{22}\mathrm{sech}^2(x_{2e}) \\ p_2 = (w_{22} - w_{12}w_{21})\mathrm{sech}(x_{2e}) + 1 \\ P_3 = 0 \end{cases} \tag{9}$$

The external stimulus input I_{ext} changes in the range of $[-I_m, I_m]$ with the time evolution, so that the values of x_{2e} is obtained and the stability of AC equilibrium point for the specified range of I_{ext} is explored numerically. By setting the parameters to $w_{21} = 2.8$,$w_{12} = -3.5$,$w_{22} = 2.4$ and $I_m = 2$,the trajectories and stability of the equilibrium points are analyzed, with the results presented in Fig. 3 and Table 2. The system's equilibrium points can be analyzed and categorized into two distinct types, i.e. stable node point (SNP) and Hopf bifurcation points

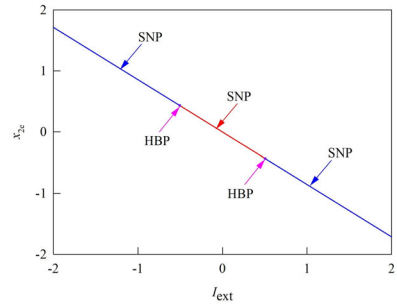

Fig. 3 Trajectory and stability of the AC equilibrium points

Table 2 AC equilibrium points

I_{ext}	Equilibrium point	Eigenvalues	Stability
− 1	$(0, 0.8571, x_{3e})$	$0, -0.9736 \pm j2.1643$	SNP
− 0.5057	$(0, 0.8571, x_{3e})$	$0, \pm j2.6771$	HBP
0	$(0, 0, x_{3e})$	$0, -0.2 \pm j2.8914$	SNP
0.5057	$(0, -0.8571, x_{3e})$	$0, \pm j2.6771$	HBP
1	$(0, -0.8571, x_{3e})$	$0, -0.9736 \pm j2.1643$	SNP

(HBP). The SNP refers to a situation where the eigenvalues of the Jacobian matrix are negative real numbers, indicating that the system is stable at this equilibrium point and will converge to it. HBP occurs when the eigenvalues of the Jacobian matrix change from purely imaginary to a complex conjugate pair, with the real part shifting from negative to positive (or vice versa). This causes the equilibrium point to become unstable, potentially leading to the formation of a periodic solution. When $I_{ext} = \pm 0.5057$, there also exist two HBP with a pair of conjugate imaginary roots and a zero eigenvalue, which are meaningless. The system exhibits complex stability attributed to the line of equilibrium points, indicating a propensity towards multistability.

For the purpose of analyzing the bifurcation routes in the proposed model (3), the midpoint method is used to discretize the system within the interval $t \in (t_{k-1}, t_k)$[32]. Thus, the mappings $\boldsymbol{P}_k (k = 1,\ 2,\ 3, \ldots)$ is given as

$$\boldsymbol{P}_k : \mathbf{x}_{k-1} \rightarrow \mathbf{x}_k \Rightarrow P_k(\mathbf{x}_{k-1})(k = 1, 2, 3, ...), \tag{10}$$

where the discrete nodes $\mathbf{x}_k = (x_{1,k}, x_{2,k}, x_{3,k})^{\mathrm{T}}$ is dispersed on the stable phase trajectory, and the corresponding algebraic equations for mappings P_k can be derived as

$$\begin{cases} x_{1,k} = x_{1,k-1} - h\bar{x}_{1,k} - hk\bar{x}_{1,k}\cos(\pi\bar{x}_{3,k})\tanh(\bar{x}_{1,k}) \\ \quad +hw_{21}\tanh(\bar{x}_{2,k}) + I_m \sin(\omega t_{k-1/2}) \\ x_{2,k} = x_{2,k-1} - h\bar{x}_{2,k} + hw_{12}\tanh(\bar{x}_{1,k}) + hw_{22}\tanh(\bar{x}_{2,k}) \\ x_{3,k} = x_{3,k-1} - h\bar{x}_{1,k} \end{cases} \tag{11}$$

where $h = t_k - t_{k-1}$ is the step of simulation time, and the midpoints $\bar{x}_{i,k} = 1/2(x_{i,k-1} + x_{i,k})(i = 1, 2, 3)$.

The mapping structure of periodic motion is indicated as

$$\boldsymbol{P} = \boldsymbol{P}_N \circ \boldsymbol{P}_{N-1} \circ \cdots \circ \boldsymbol{P}_2 \circ \boldsymbol{P}_1 : \mathbf{x}_0 \rightarrow \mathbf{x}_N \tag{12}$$

Therefore, $\mathbf{x}_N$ is denoted as

$$\mathbf{x}_N = \boldsymbol{P}\mathbf{x}_0 = \boldsymbol{P}_N \circ \boldsymbol{P}_{N-1} \circ \cdots \circ \boldsymbol{P}_2 \circ \boldsymbol{P}_1\mathbf{x}_0, \tag{13}$$

where $\mathbf{x}_N = \boldsymbol{P}_N\mathbf{x}_{N-1}, \mathbf{x}_{N-1} = \boldsymbol{P}_{N-1}\mathbf{x}_{N-2}, \ldots, \mathbf{x}_2 = \boldsymbol{P}_2\mathbf{x}_1, \mathbf{x}_1 = \boldsymbol{P}_1\mathbf{x}_0$, Eq. (13) should satisfy Eq. (12) for the mappings $\boldsymbol{P}_k$

$$\mathbf{g}_k(\mathbf{x}_{k-1}, \mathbf{x}_k) = 0 \tag{14}$$

where $\mathbf{g}_k(\mathbf{x}_{k-1}, \mathbf{x}_k) = (g_{1,k}(\mathbf{x}_{k-1}, \mathbf{x}_k), g_{2,k}\ (\mathbf{x}_{k-1}, \mathbf{x}_k), g_{3,k}\ (\mathbf{x}_{k-1}, \mathbf{x}_k))^{\mathrm{T}}$, and Eq. (13) is rewritten by

$$\begin{cases} g_{1,k}(\mathbf{x}_{k-1}, \mathbf{x}_k) = x_{1,k} - M_1 \\ g_{2,k}(\mathbf{x}_{k-1}, \mathbf{x}_k) = x_{2,k} - M_2\,, \\ g_{3,k}(\mathbf{x}_{k-1}, \mathbf{x}_k) = x_{3,k} - M_3 \end{cases} \tag{15}$$

where M_i denotes the right-hand part of the $i-$th equation in Eq. (11). And the periodic conditions for the system is

$$\left(x_{1,mN}, x_{2,mN}, x_{3,mN}\right)^{\mathrm{T}} = \left(x_{1,0}, x_{2,0}, x_{3,0}\right)^{\mathrm{T}} \tag{16}$$

Assume a small perturbation $\Delta\mathbf{x}_k$ close to $\mathbf{x}_k^*\left(\text{i.e.}\mathbf{x}_k = \mathbf{x}_k^* + \Delta\mathbf{x}_k\right)$, the linearization of Eq. (14) is

$$\begin{aligned} &\frac{\partial \mathbf{g}_k(\mathbf{x}_{k-1}, \mathbf{x}_k)}{\partial \mathbf{x}_{k-1}}\bigg|_{\left(\mathbf{x}_{k-1}^*, \mathbf{x}_k^*\right)} \Delta\mathbf{x}_{k-1} \\ &+ \frac{\partial \mathbf{g}_k(\mathbf{x}_{k-1}, \mathbf{x}_k)}{\partial \mathbf{x}_k}\bigg|_{\left(\mathbf{x}_{k-1}^*, \mathbf{x}_k^*\right)} \Delta\mathbf{x}_k \\ &= 0 \end{aligned} \tag{17}$$

For the structure of discrete mappings, the variables of disturbance $\Delta\mathbf{x}_N$ is expressed as

$$\Delta\mathbf{x}_N = DP\Delta\mathbf{x}_0 = DP_N \cdot DP_{N-1} \cdot \cdots \cdot DP_2 \cdot DP_1\Delta\mathbf{x}_0 \tag{18}$$

and the Jacobian matrix DP of Eq. (14) in periodic motions is rewritten specifically as

$$DP = \left[\frac{\partial \mathbf{x}_N}{\partial \mathbf{x}_0}\right]_{(\mathbf{x}_0^*, \mathbf{x}_1^*, \cdots \mathbf{x}_{N-1}^* \mathbf{x}_N^*)} = DP_N \cdot DP_{N-1} \cdot \cdots \cdot DP_2 \cdot DP_1 = \prod_{k=N}^{1} \left[\frac{\partial \mathbf{x}_k}{\partial \mathbf{x}_{k-1}}\right]_{(\mathbf{x}_{k-1}^* \mathbf{x}_k^*)} \tag{19}$$

Upon, the three eigenvalues of matrix in Eq. (18) are solved through:

$$\det(DP - \lambda \mathbf{I}_{3\times 3}) = 0 \tag{20}$$

Additionally, the stability of periodic motions is elucidated through the determined eigenvalues, with the guidelines outlined as follows: (1) if all $|\lambda_p| < 1 (p = 1, 2, 3)$, the period-m motion is stable. (2) if at least one $|\lambda_p| > 1$, $(p = 1, 2, 3)$, the period-m motion is unstable. And the classification of the bifurcation points can be judged by: (1) if $\lambda_p = 1$ and $|\lambda_q| < 1 (p, q \in \{1, 2, 3\}, p \neq q)$, saddle-node bifurcation (SN) happens. (2) if $\lambda_p = -1$, and $|\lambda_q| < 1 (p, q \in \{1, 2, 3\}, p \neq q)$, period doubling bifurcation (PD) happens.

Therefore, the dynamical behaviors can be analyzed through the eigenvalues, and the mechanism of the extreme multistable and firing phenomenon will be better illustrated from a novel perspective through the discrete mapping method.

3 Dynamic behavior analysis

In this section, the MHNN's dynamics will be investigated through discrete mapping methods, in which bifurcation trees and Lyapunov exponents varying the self-coupling strength are developed.

3.1 Coexisting bifurcation behaviors

To explore the impact of self-coupling strength k on the dynamic behavior of the MHNN system, with system parameters set as $\omega = 0.84$, $I_m = 2, w_{21} = 2.8, w_{12} = -3.5, w_{22} = 2.4$, Fig. 3 illustrates the relationship between the numerical bifurcation diagram and Lyapunov exponent spectrum as the self-coupling strength k ranging from 4.85 to 7.45. The bifurcation behavior of internal state variable of memristor x_3 is shown in Fig. 4a, where the red, blue, green, pink, cyan and brown colored trajectories belong to the initial conditions $(x_1, x_2, x_3) = (4, 0, 0)$, $(5.9, 0, 0)$, $(7, 0, 0)$, $(8, 0, 0)$, $(9, 0, 0)$ and $(11, 0, 0)$, respectively. It is worth noting that as the initial condition changes, the system variable x_3 exhibits infinite similar coexisting bifurcation routes, in which only six routes are shown here. In the meantime, the bifurcation diagram of the membrane potentials x_1 and x_2 are also emulated, as depicted in Fig. 4b and c, where the red and blue colored trajectories separately correspond to initial conditions $(x_1, x_2, x_3) = (1, 0, 0)$, $(5, 0, 0)$. However, regardless of how the initial condition change, x_1 and x_2 exhibits only two similar bifurcation routes, which means that the transition of firing modes has similarities. As shown in Fig. 4d, the Lyapunov exponent spectra (LEs) is plotted relative to the bifurcation diagram in Fig. 4a–c, from which it can be seen that the dynamics characterized in the LEs are identical to those illustrated in the bifurcation diagrams.

To probe the mechanism of bifurcation of the system further, the discrete mapping method is adopted to acquire the analytical solution of the system. Under the accuracy $\varepsilon = O(h^3) < 10^{-9}$ and the time step $h < 10^{-3}$, the discrete nodes $(x_{1,k}, x_{2,k}, x_{3,k})^{\mathrm{T}}$ are obtained. Consider a set of coexisting bifurcation routes in the lowermost part of Fig. 4a, the numerical and analytical bifurcation tree for that part is given in Fig. 5a and b. Figure 5a shows the numerical results, while Fig. 5b displays the analytical results. The period-m motion is marked as "P-m". In further, for all bifurcation trees drawn in this paper, solid and short dashed lines correspond to stable and unstable periodic motions, and coexisting periodic motions are indicated by different colors.

In Fig. 5a, the solid line represents the observed stable periodic motion, whereas the unstable periodic motion appears as scattered chaotic points in the numerical bifurcation tree. However, both stable and unstable periodic motions of the system are distinctly visible in the analytical bifurcation tree shown in Fig. 5b. In the simulation interval $k \in (4.85, 7.45)$, the system appears to have complex bifurcation paths, including switching between stable and unstable periodic motions and different bifurcation points. When $k = 4.85$, the system exhibits stable symmetric P-1 motion. As k increases to 5.09, PD bifurcation occurs. On the one hand, the system transitions from coexisting stable P-1 motion to stable P-2 motion. On the

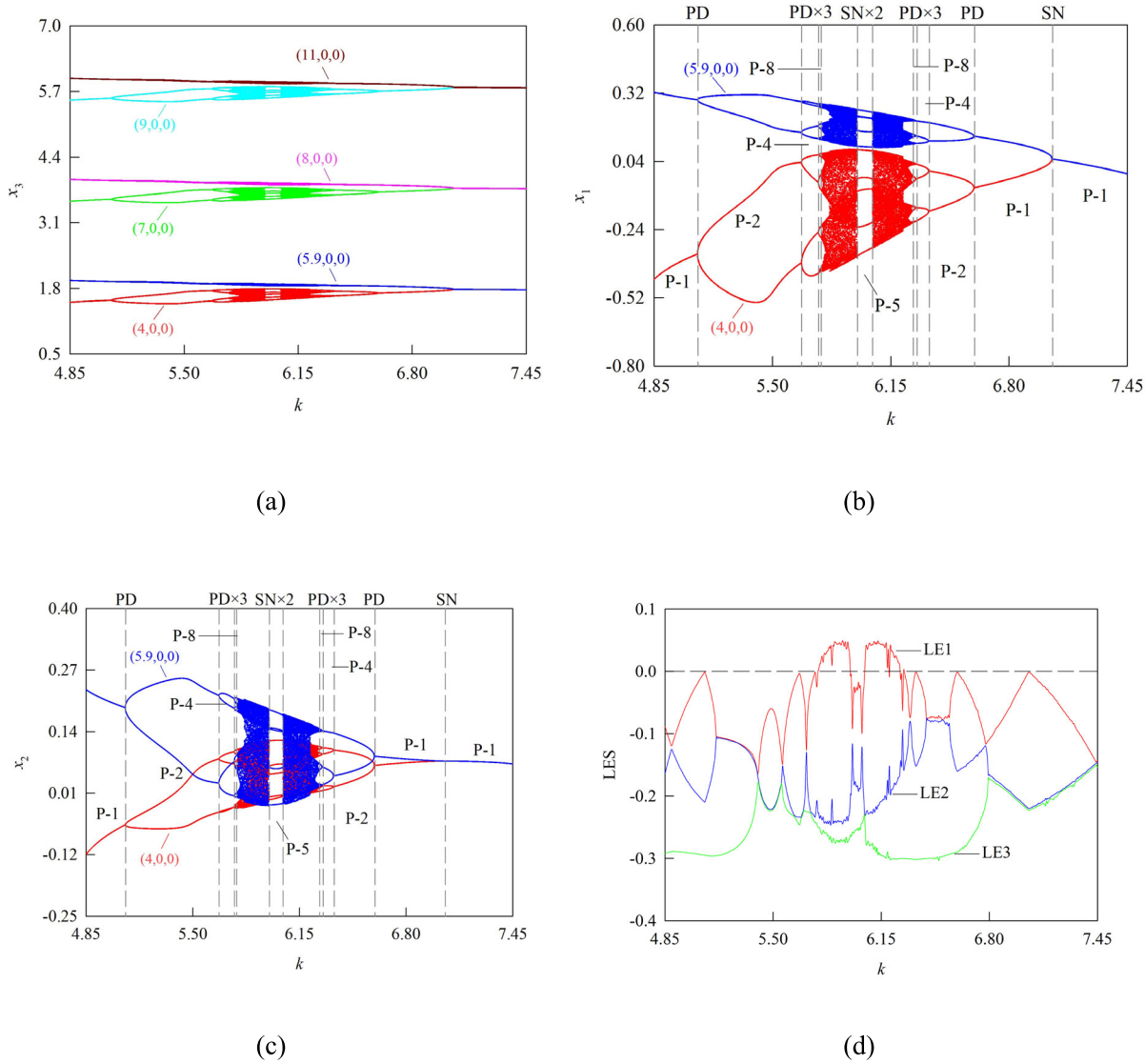

Fig. 4 Coexisting bifurcation under the different initial conditions: **a**, **b** and **c** bifurcation diagram of x_3,x_1 and x_2, **d** Lyapunov exponent spectra ($\omega = 0.84, I_m = 2, w_{21} = 2.8, w_{12} = -3.5, w_{22} = 2.4$)

other hand, coexisting unstable P-1 motion also emerges at this PD bifurcation point. As the coupling strength k increase to 5.768, the system presents a forward period-doubling bifurcation process, in which three PD bifurcation emerge at $k = 5.66, 5.753$ and 5.768. Similarly, the coexisting unstable P-2 to P-8 motions are generated at the corresponding bifurcation points. When $k \in (5.768, 5.966)$, it is evident from the numerical bifurcation diagram that this is a chaotic region where rich unstable periodic motions, such as P-1, 2, 4 and 8 motions simultaneously exist. After k is raised to 5.966, a periodic window emerges, which concludes at $k = 6.05$. At both ends of this periodic window, SN bifurcation points are present. Additionally, coexisting stable and unstable P-5 motions will appear and disappear at these boundaries. Similar to the system entering chaotic area through, at the end of periodic window, the system is about to evolve into a chaotic region where $k \in (6.05, 6.274)$. As k continues to increase, the system evolves from chaos to a periodic motion after reverse period-doubling bifurcation process in the range of $k \in (6.274, 7.04)$ and the

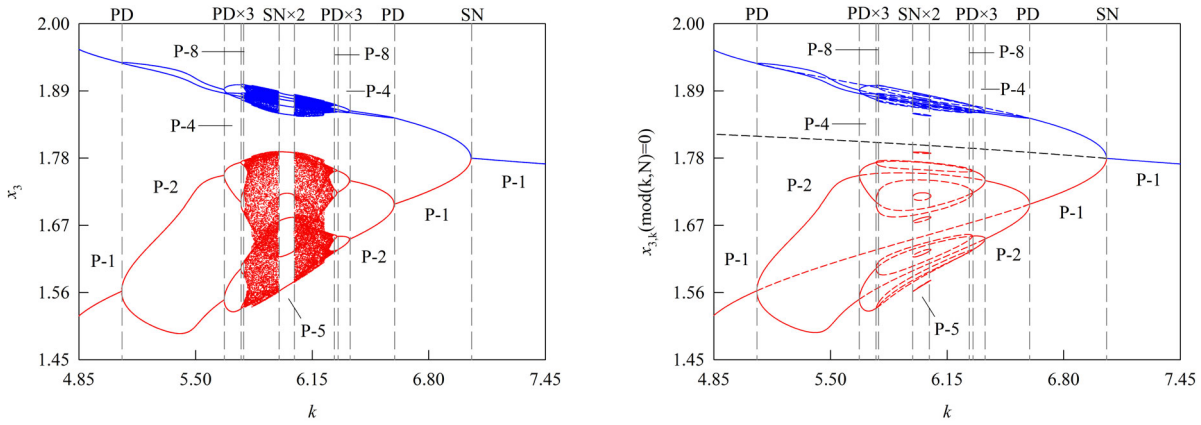

Fig. 5 Global coexisting bifurcation trees of x_3 varying with coupling strength k: **a** numerical solution, **b** analytical solution ($\omega = 0.84, I_m = 2, w_{21} = 2.8, w_{12} = -3.5, w_{22} = 2.4$)

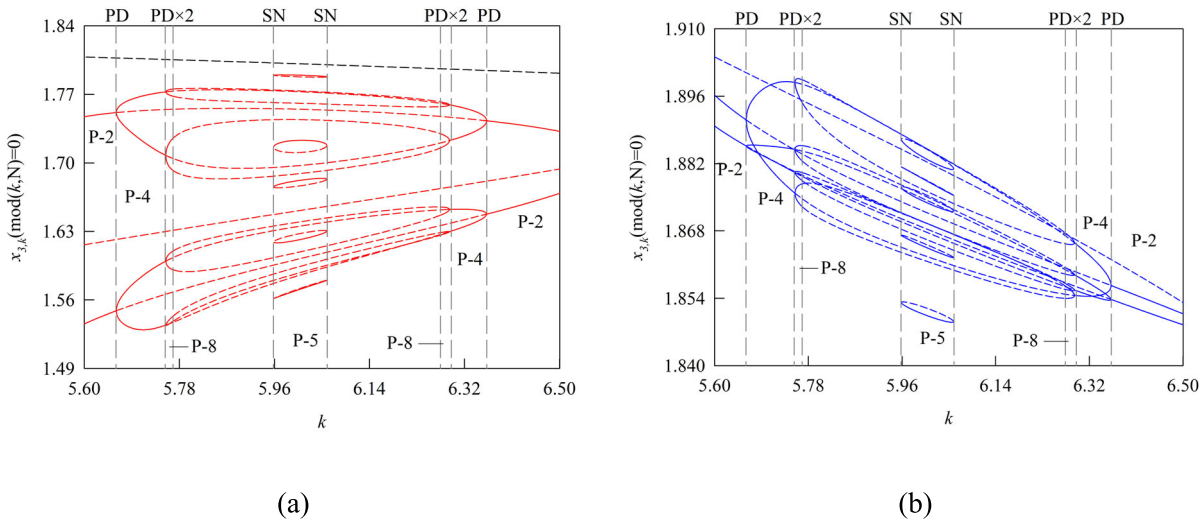

Fig. 6 Zoomed view of coexisting analytical bifurcation trees in $k \in (5.60, 6.50)$

four PD bifurcation points can be observed at $k = 6.274, 6.295, 6.36$ and 6.61. In parallel, the unstable P-8, 4, 2, and 1 motions terminate at the corresponding PD bifurcation points. It is noteworthy a SN bifurcation, where there is a SN bifurcation occurs at the intersection of the two coexisting bifurcation routes, where unstable P-1 motion also emerges which is marked by black dash. And then the red route and blue route completely overlap for $k \in (7.04, 7.45)$,which means that the trajectories of attractors are the same in the case of different initial values.

To provide a clearer illustration of the coexisting bifurcation routes, Fig. 6 presents a zoomed view. Figure 6a depicts the red bifurcation routes, while Fig. 6b illustrates the blue bifurcation routes. The stable P-4 motions coexist within the ranges of $k \in (5.66, 5.753)$ and $(6.295, 6.36)$, whereas unstable one coexists in the range of $k \in (5.573, 6.295)$. Likewise, the stable P-8 motions coexist in the regions of $k \in (5.753, 5.768)$ and $(6.274, 6.295)$, while unstable one coexists in the range of $k \in (5.768, 6.274)$. Table 3 provides additional details regarding the stability of periodic motion and bifurcation points,

where'Left'denotes the type of bifurcation point on the left side of the region, and'Right'indicates the type of bifurcation point on the right side. Additionally,'S'represents stable, while'U'represents unstable. Compared to numerical results, the analytical solution offers comprehensive bifurcation routes and an independent periodic motion of the system, enabling researchers to thoroughly analyze the intricate bifurcation mechanism and stability.

Table 3 Period-1 to period-8 of MHNN

Period-m	k	Left	Right	Stability
P-1	$(4.85 \rightarrow 5.09)$	–	PD	S
	$(6.61 \rightarrow 7.04)$	PD	SN	S
	$(7.04 \rightarrow 7.45)$	SN	–	S
	$(4.85 \rightarrow 7.04)$	–	SN	U
	$(5.09 \rightarrow 6.61)$	PD	PD	U
P-2	$(5.09 \rightarrow 5.66)$	PD	PD	S
	$(6.36 \rightarrow 6.61)$	PD	PD	S
	$(5.66 \rightarrow 6.36)$	PD	PD	U
P-4	$(5.66 \rightarrow 5.753)$	PD	PD	S
	$(6.295 \rightarrow 6.36)$	PD	PD	S
	$(5.573 \rightarrow 6.295)$	PD	PD	U
P-5	$(5.966 \rightarrow 6.05)$	SN	SN	S
	$(5.966 \rightarrow 6.05)$	SN	SN	U
P-8	$(5.753 \rightarrow 5.768)$	PD	PD	S
	$(6.274 \rightarrow 6.295)$	PD	PD	S
	$(5.768 \rightarrow 6.274)$	PD	PD	U

To explain the relationship between bifurcation phenomena and eigenvalues in detail, the real part and magnitude of the eigenvalues corresponding with Fig. 5a are offered in Fig. 7a and b, where the red short dash line and black solid line represent unstable and stable periodic motion respectively. Apparently, the total evolution consists mainly of the switching of stable and unstable periods, and the occurrence of PD and SN bifurcations. Relatively simple cases involve periodic motions with regular transitions between stable and unstable states. The bifurcation route of period-8 is more complex. As k increases from 4.85 to 7.45, the stable period-8 motion first emerges at $k = 5.753$, where the period-4 motion transitions to an unstable state as λ_3 from a larger to a smaller value. Then period-8 motion quickly transitions from a stable state to an unstable state at about $k = 5.768$ with $\lambda_3 = -1$, where the period-doubling bifurcation occurs. With the increase of parameter k, there will be a periodic window, the ends of which are also the start and end points of the stable and unstable period-5 motions. Since λ_3 satisfies $\lambda_3 = 1$, the bifurcation points are saddle-node bifurcations at the ends of the periodic window, which are $k = 5.966$ and $k = 6.05$. Due to an associated reverse tendency, the period-8 motion returns to a stable state at a specific parameter value, subsequently transitioning into stable period-4 and period-2 states at $k = 6.295$ and $k = 6.36$ through period-doubling bifurcations. Throughout this process, $\lambda_3 = -1$ is consistently satisfied. However, all these periodic routes remain unstable within the

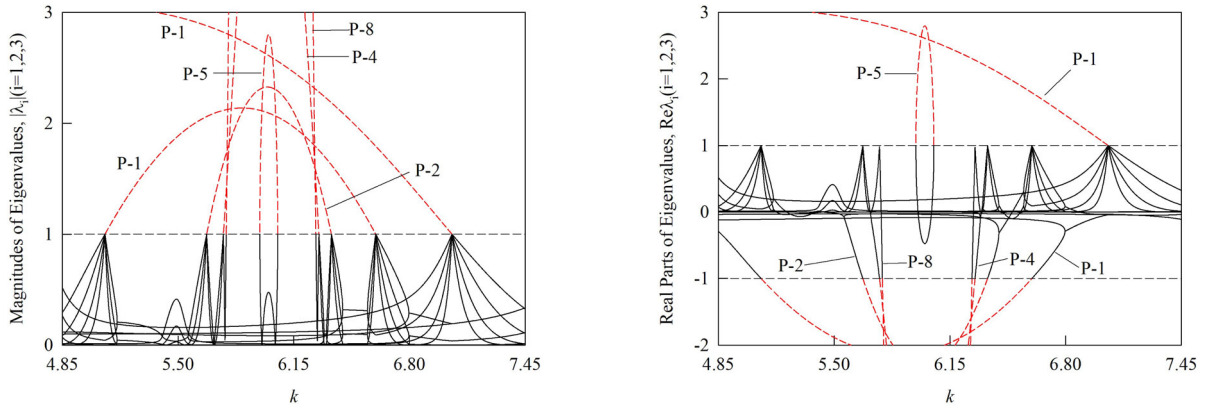

Fig. 7 Eigenvalues of system: **a** magnitudes, **b** real parts

chaotic region when $\lambda_3 < -1$. A saddle-node bifurcation occurs at $k = 7.04$ when two coexisting period-1 motions converge at one place. Therefore, with the help of the eigenvalues, the firing phenomenon and stability of the neural network have been accurately identified. According to the guidelines given in Sect. 2, the stability of each periodic route, the exact bifurcation location and the type of bifurcation points are listed in Table 3.

3.2 Coexisting attractors

Corresponding to the bifurcation diagrams in Fig. 4 and fixing $x_2(0) = 0$,$x_3(0) = 0$, the initial condition bifurcation diagrams for the range $0 \leq x_1(0) \leq 20$ are given in Fig. 8 by considering $k = 4.85$ and 6.15, which correspond to periodic and chaotic states, respectively. As can be seen in Fig. 8a and b, there are only two states for x_1 and x_2, regardless of whether they are in a periodic or chaotic state. However, as can be seen in Fig. 8c and d, the bifurcation diagram exhibits an infinite stepwise increasing trend as $x_1(0)$ increases, with one planar position matching an independent periodic attractor or chaotic attractor. What is fascinating is that, for x_1 and x_2, there are always only two states, no matter how $x_1(0)$ changes, while for x_3 there are an infinite number of states.

Based on the results of the bifurcation diagrams with related to the initial condition, varying x_1 corresponds to changing the membrane potential. As

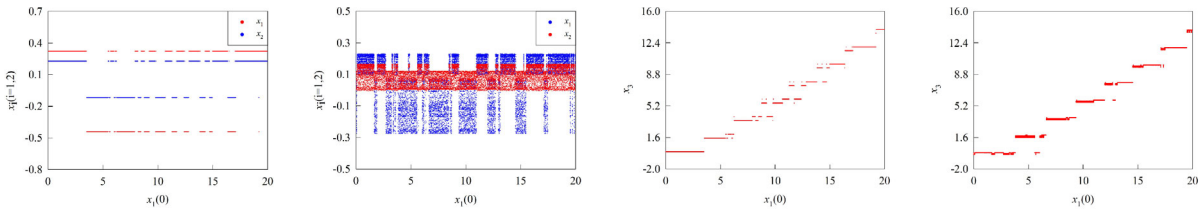

Fig. 8 Initial condition bifurcation diagrams: **a** and **b** the variable of $x_{1,2}$ at $k = 4.85$ and 6.15 respectively, **c** and **d** the variable of x_3 at $k = 4.85$ and 6.15 respectively

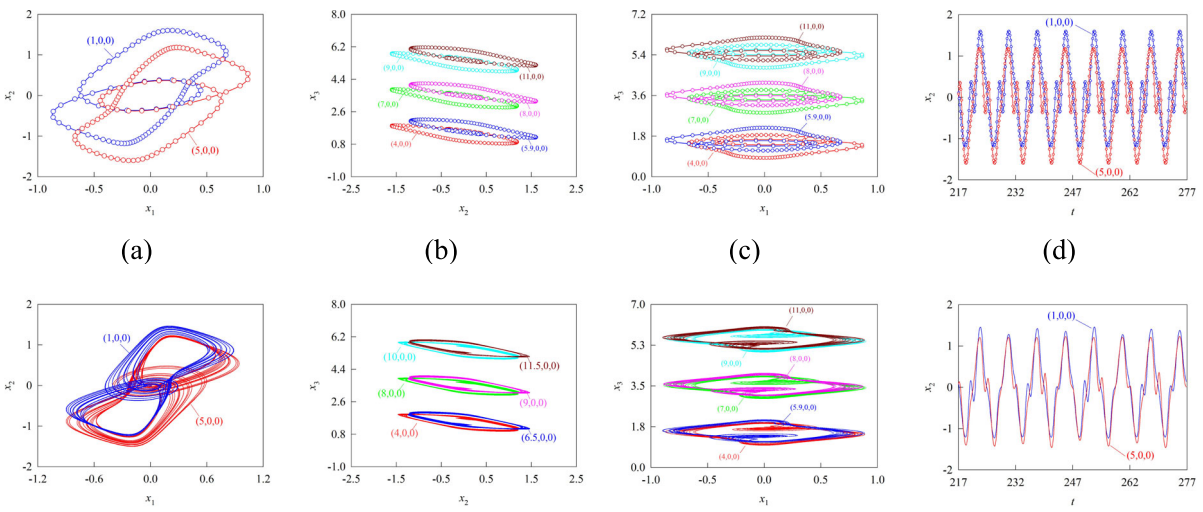

Fig. 9 Coexisting attractors and time sequences: period-1 at $k = 4.85$**a** attractors in the $x_1 - x_2$ plane, **b** attractors in the $x_2 - x_3$ plane, **c** attractors in the $x_1 - x_3$ plane, **d** periodic spiking firing; chaos at $k = 6.15$, **e** attractors in the $x_1 - x_2$ plane, **f** attractors in the $x_2 - x_3$ plane, **g** attractors in the $x_1 - x_3$ plane, **h** chaotic spiking firing

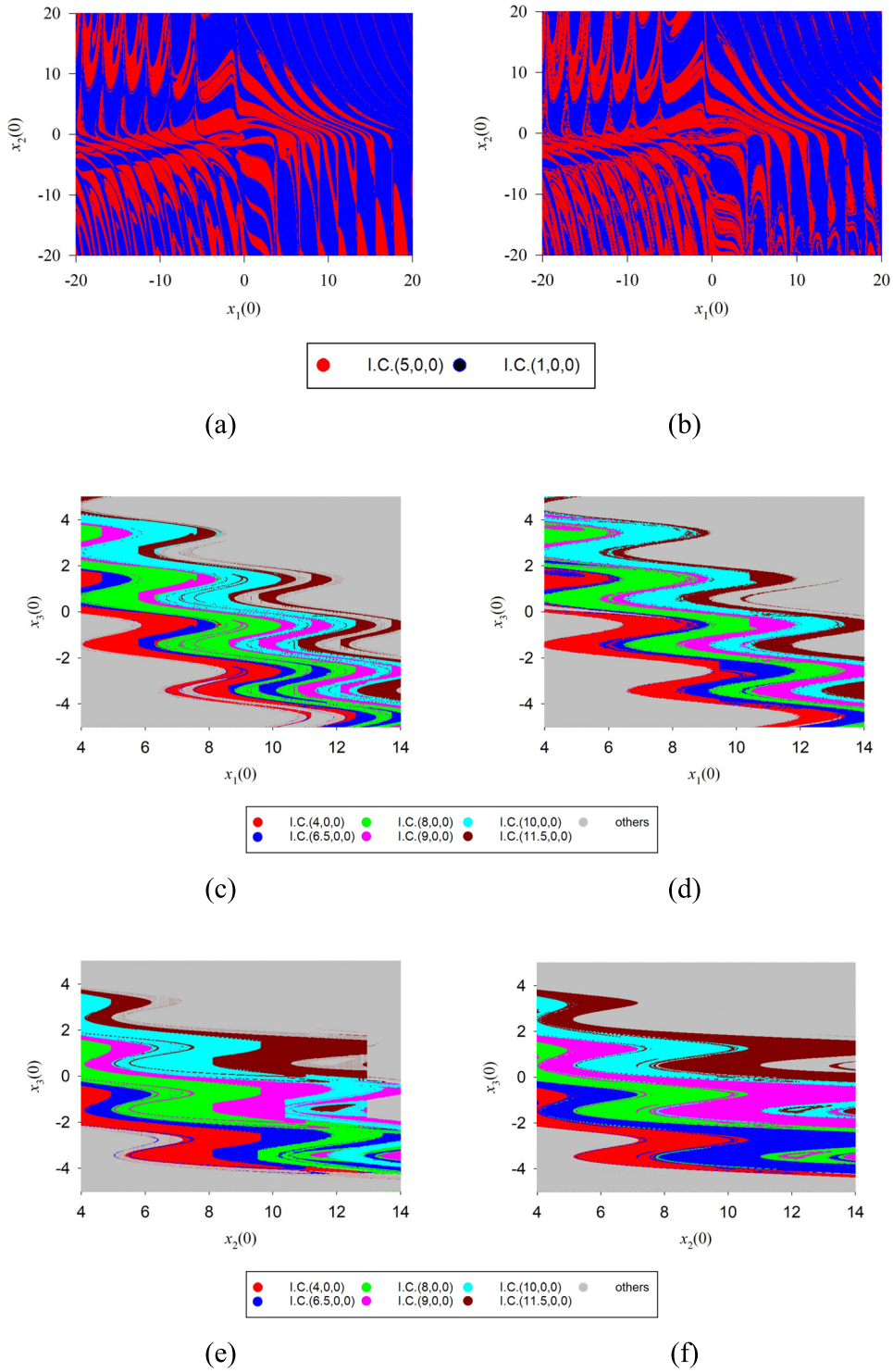

Fig. 10 Local attraction basin: in the $x_1(0) - x_2(0)$ plane. **a** at $k = 4.85$, **b** at $k = 6.15$; in the $x_1(0) - x_3(0)$ plane, **c** at $k = 4.85$, **d** at $k = 6.15$; in the $x_2(0) - x_3(0)$ plane, **e** at $k = 4.85$, **f** at $k = 6.15$

shown in Fig. 9, this variation causes the system to produce periodic and chaotic attractors of the same type but located at different positions in the $x_1 - x_2$ and $x_2 - x_3$ plane. The specific initial values have been labeled on the figure. The time sequences about neuron membrane potential x_2 are also explored at different k,as depicted in Fig. 9d and h. Consider initial values $(x_1, x_2, x_3) = (1, 0, 0)$(blue) and $(5, 0, 0)$(red), with $k = 4.85$, the model shows regular period-1 spiking firing pattern. When k increases to 6.15, the model turns to chaotic spiking pattern. In Fig. 9a, b, c and d, the solid line is the result obtained through the conventional numerical method, while the circles denote the outcomes derived from the analytical method. Notably, there is a significant concurrence between the two sets of results, indicating a high level of agreement. On the other hand, in order to demonstrate the coexisting attractors, local attraction basins corresponding to Fig. 9a–h are given in Fig. 10a–f. Different colors are used to draw the basin of attraction and to delineate the plane of initial condition (I.C.), the colors corresponding to the colors of the attractors. As a result, this attraction basin has a beautifully streamlined structure, and it can be observed from the attraction basin that the network proposed in this study exhibits multistable firing states.

3.3 Coexisting unstable periodic orbits

From the previous analytical method, the coexisting bifurcation trees have been solved. In this part, the phase trajectory diagrams will provide a fresh perspective to understand the stability of periodic motion. Consider parameters of $\omega = 0.84$, $I_m = 2$,$w_{21} = 2.8$,$w_{12} = -3.5$, $w_{22} = 2.4$, the phase trajectories of coexisting unstable periodic orbits in $x_2 - x_3$ plane are illustrated in Fig. 11. T is set as the time required to complete one periodic motion, i.e. T = 2 π/ω. The simulation time is set to $(0, 96T)$, red, blue, and black circles indicate the analytical solution for $(0, mT)$, solid lines of the corresponding color are the numerical solution for $(0, mT)$, and thin gray solid lines are the numerical solution for $(mT, 96T)$. The initial conditions employed in the numerical method correspond to those of the exact unstable periodic motions derived from the analytical approach, which are $(x_1, x_2, x_3) = (0.19, 0.11, 1.87)$,$(-0.14, 0.045, 1.66)$ and $(0.13, 0.079, 1.8)$, respectively, and the simulation results of the coexisting unstable period-1 orbits are presented in Fig. 11a. It can be seen that in the first T, the solid line and the circle are highly overlapped. Due to the iterative computation error in the numerical method, the motion trajectory of the system will gradually deviate from the original unstable periodic orbit as the simulation time is prolonged. Similar divergence processes exist for other coexisting unstable periodic orbits. From the phase trajectories, it can be seen that there are three coexisting unstable period-1 orbits, while there are only two coexisting unstable period-2, 4, 5 orbits.

When parameters are set to $\omega = 0.84$, $I_m = 2$,$w_{21} = 2.8$,$w_{12} = -3.5$, $w_{22} = 2.4$, the transition from an unstable period-1 orbit to a stable period-2 orbit is illustrated phase trajectory, with initial values of $(x_{10}, x_{20}, x_{30}) = (-0.23, 0.0035, 1.62)$ and $(-0.24, 0.15, 1.9)$ selected, as depicted in Fig. 12a and b. The black solid line represents the unstable period-1 orbit, whereas the red and blue solid lines denote the stable period-2 orbit, as determined through numerical methods. The red and blue circles correspond to the analytical solutions, while the thin gray solid line illustrates the intermediate transition process between the unstable period-1 orbit and the stable period-2 orbit. Additionally, the transition of the neuron

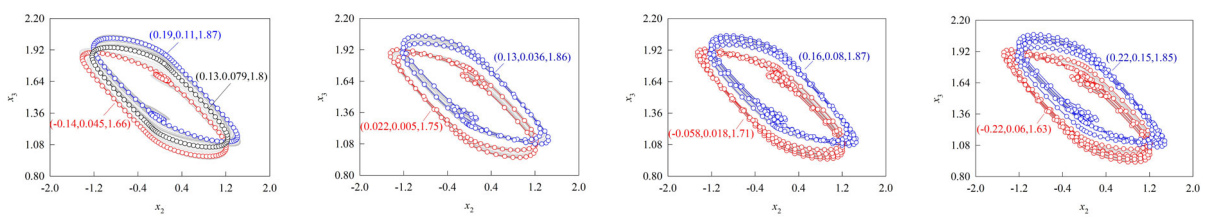

Fig. 11 Coexisting unstable periodic orbits at $k = 6.15$: **a** period-1, **b** period-2, **c** period-4, **d** period-5

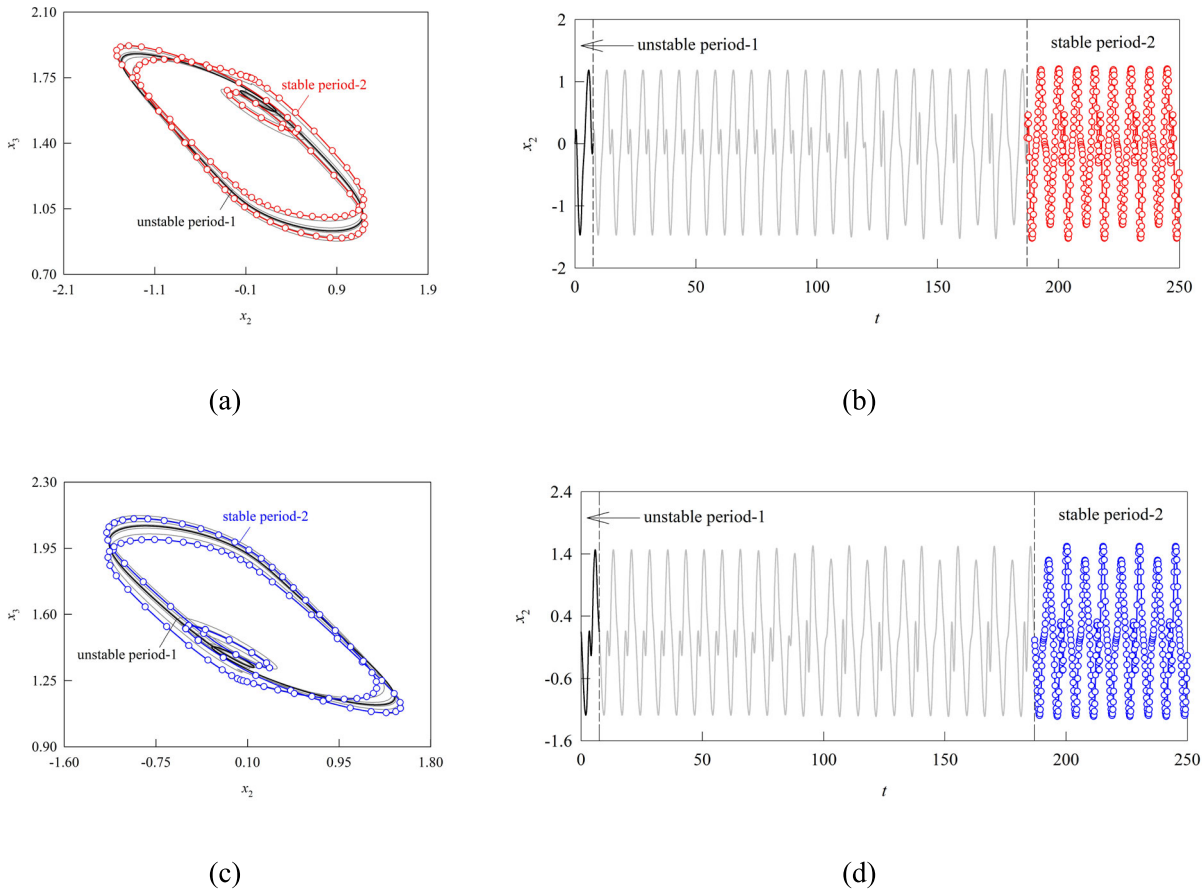

Fig. 12 The transition of unstable period-1 orbit to stable period-2 orbit at $k = 5.6$: **a** and **c** phase trajectories, **b** and **d** corresponding time sequence

from an unstable firing mode to a stable one is depicted through the time sequence analysis, as presented in Fig. 12c and d.

4 Attractor control

In the case of extreme multistability, the system exhibits an infinite number of coexisting attractors, where even slight variations in initial conditions can result in entirely different dynamical evolutions. Investigating attractor control is crucial for selecting desired dynamical states from numerous possibilities, thereby enhancing the system's controllability. System (3) demonstrates extreme multistability in a single direction by adjusting its initial value; thus, the introduction of a rotation matrix is proposed to enable the modified system to generate infinitely many attractors in any direction within the two-dimensional plane. Moreover, rotational control can alter the amplitude without affecting the Lyapunov exponent [42], meaning that the Lyapunov exponent remains constant and the eigenvalues of the rotating system do not change. Incorporating a rotation matrix into the neuronal system not only preserves the original multistability properties but also enhances information encoding capabilities by leveraging the attractor rotation method [43, 44]. The following discussion provides a comprehensive analysis of the adjustable rotation control approach, which depends on a single independent parameter and the selected initial values.

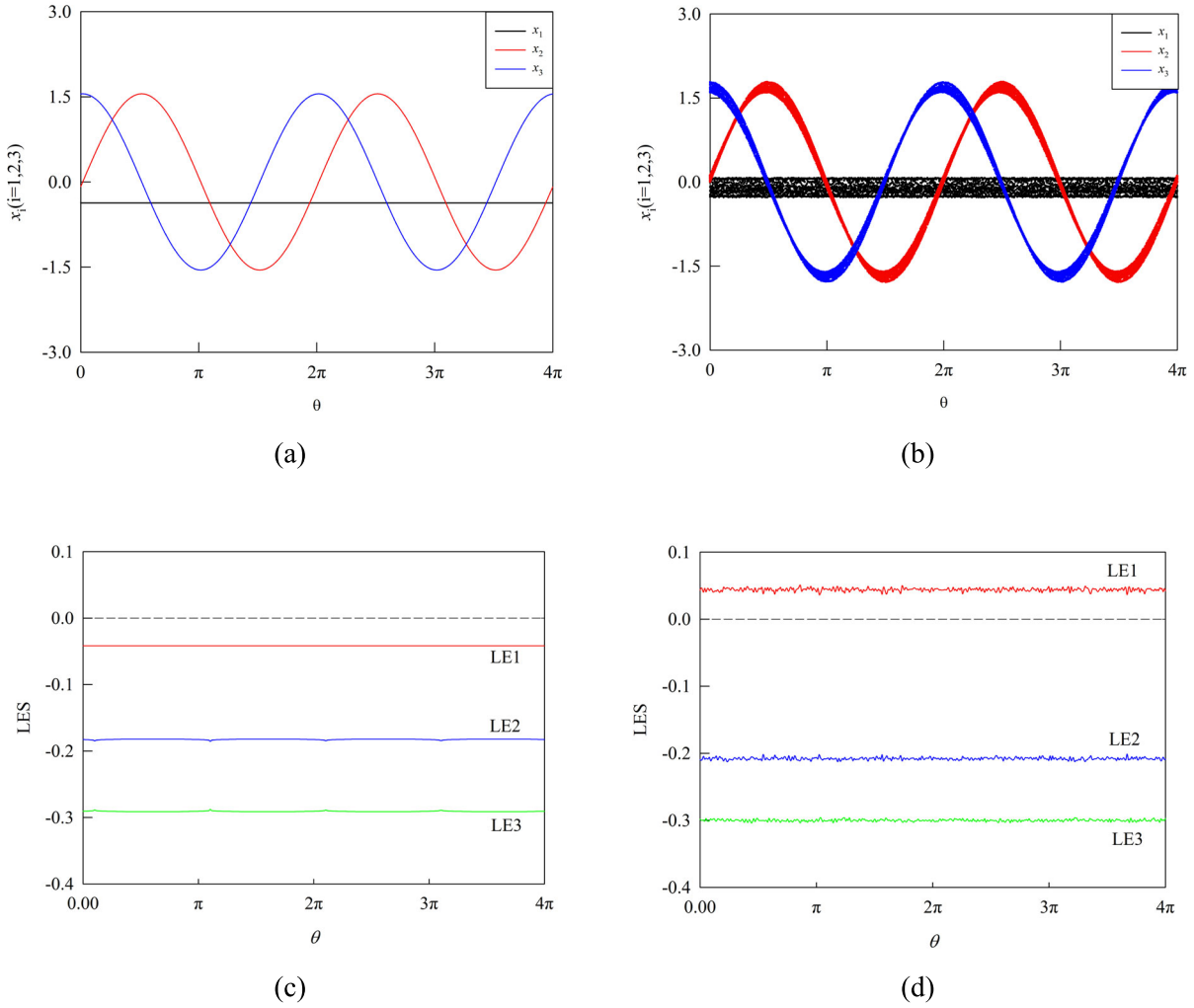

Fig. 13 Bifurcation diagram and corresponding Lyapunov exponent spectra when the control parameter θ is to change within the range $(0, 4\pi)$: **a** and **c** $k = 4.85$, **b** and **d** $k = 6.15$

A 3-D matrix rotating around the x_1-axis is analyzed on the basis of system (3)

$$\begin{pmatrix} x \\ y \\ z \end{pmatrix} = \begin{pmatrix} 1 & 0 & 0 \\ 0 & \cos\theta & -\sin\theta \\ 0 & \sin\theta & \cos\theta \end{pmatrix} \begin{pmatrix} x_1 \\ x_2 \\ x_3 \end{pmatrix} \tag{21}$$

The new differential equation is as follows

$$\begin{aligned} \dot{x} &= \dot{x}_1 \\ \dot{y} &= \dot{x}_2 \cos\theta - \dot{x}_3 \sin\theta \\ \dot{z} &= \dot{x}_2 \sin\theta + \dot{x}_3 \cos\theta \end{aligned} \tag{22}$$

Lastly, the control equation based on the system (3) can be derived as

$$\begin{aligned} \dot{x}_1 &= -x_1 + kx_1 \cos(\pi T_3) \tanh(x_1) \\ &\quad + w_{21} \tanh(T_2) + I_m \sin(\omega t) \\ \dot{x}_2 &= \cos\theta(-T_2 + w_{12} \tanh(x_1) \\ &\quad + w_{22} \tanh(T_2)) + x_1 \sin\theta \\ \dot{x}_3 &= -\sin\theta(-T_2 + w_{12} \tanh(x_1) \\ &\quad + w_{22} \tanh(T_2)) + x_1 \cos\theta \end{aligned} \tag{23}$$

where

$$\begin{cases} T_1 = \cos\theta x_2 - \sin\theta x_3 \\ T_2 = \sin\theta x_2 + \cos\theta x_3 \end{cases} \tag{24}$$

Set the system rotation angle parameter to change in $(0, 4\pi)$, fix the other parameters as $\omega = 0.84$,

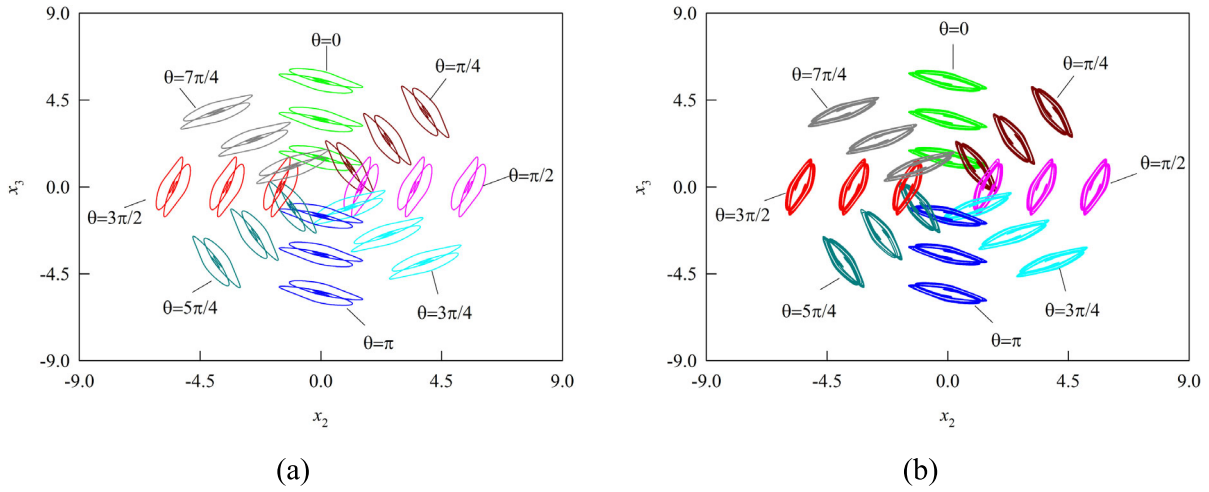

Fig. 14 Rotation control attractors at different angels and initial conditions: **a** period-1 attractors, **b** chaotic attractors

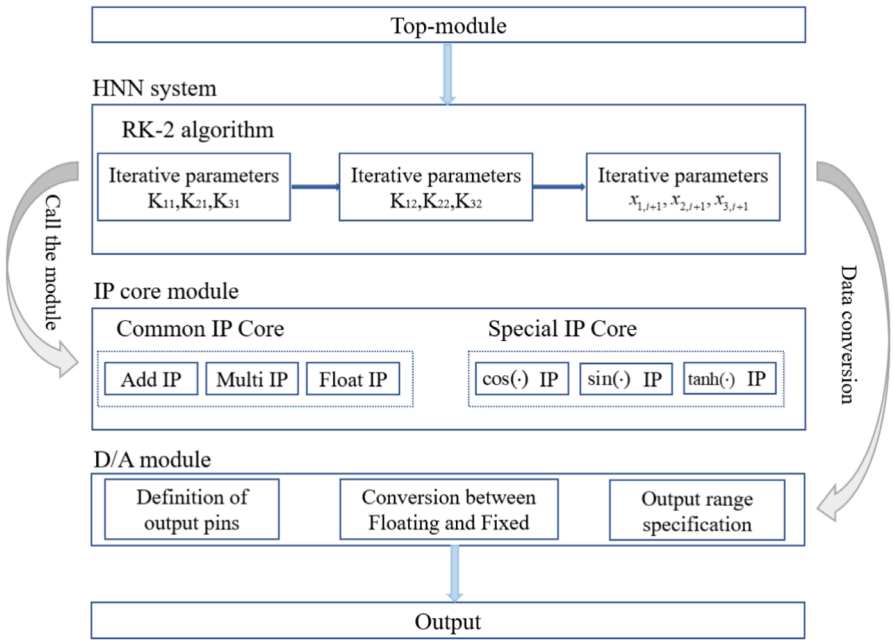

Fig. 15 Verilog programming framework

$I_m = 2$, $w_{21} = 2.8$,$w_{12} = -3.5$, $w_{22} = 2.4$ and the initial condition is $(5, 0, 0)$, the bifurcation diagram and Lyapunov exponents about the rotation angle θ is shown in Fig. 13. When the angle parameter θ changes, the variables of the system evolve sinusoidally with a period of 2π. From Fig. 13a and c, when $k = 4.85$ any change in the angle does not cause chaotic solution or any other periodic solution of the system, which is always in a period one state. From Fig. 13b and d, it can be seen that any change in the angle does not give rise to a periodic solution of the system when $k = 6.15$, the system remains in a chaotic state at all times. It can be seen from Fig. 13c and d that the Lyapunov exponent is not affected by rotation, which can maintain the distance from any point to the origin in phase space [45]. Rotating attractors in the $x_2 - x_3$ plane at various angles and initial values are depicted in Fig. 14. Attractors of the same color but located at different positions are obtained by varying the initial values while maintaining a constant angle.

This observation indicates that adjusting the rotation angle enables the positioning of attractors at various locations within the phase plane without altering their shape, demonstrating that the introduction of the rotation matrix preserves the original system's dynamical properties. In comparison to system (3), the system incorporating rotational control allows for attractor positioning in any desired direction by modifying the rotation angle parameter and initial conditions. Furthermore, each attractor obtained through rotational control can be systematically analyzed using the discrete mapping method proposed in the literature, providing deeper insights into the system's dynamical behavior.

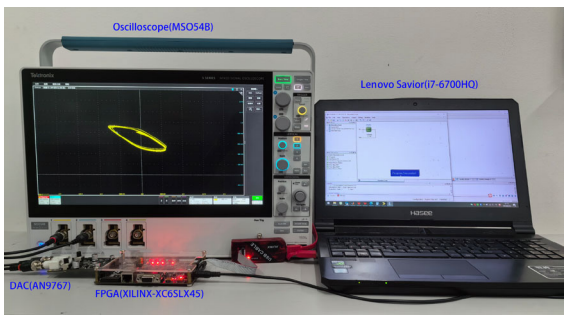

Fig. 16 Hardware platform for FPGA

5 FPGA realization

Implementing neural networks in hardware presents a highly promising research avenue within neuromorphic engineering applications. However, the inherent nonlinearity of the function poses substantial challenges for analog hardware circuits in accurately realizing the model. Furthermore, the multistable behavior exhibited by this model is highly sensitive to the predetermined initial conditions of its dynamic elements. In analog circuits, precisely defining these initial conditions is often challenging, thereby constraining their ability to accurately replicate the model's behavior. Consequently, FPGA-based digital hardware platforms emerge as a more effective solution for implementing the model, offering enhanced capabilities in capturing the phenomenon

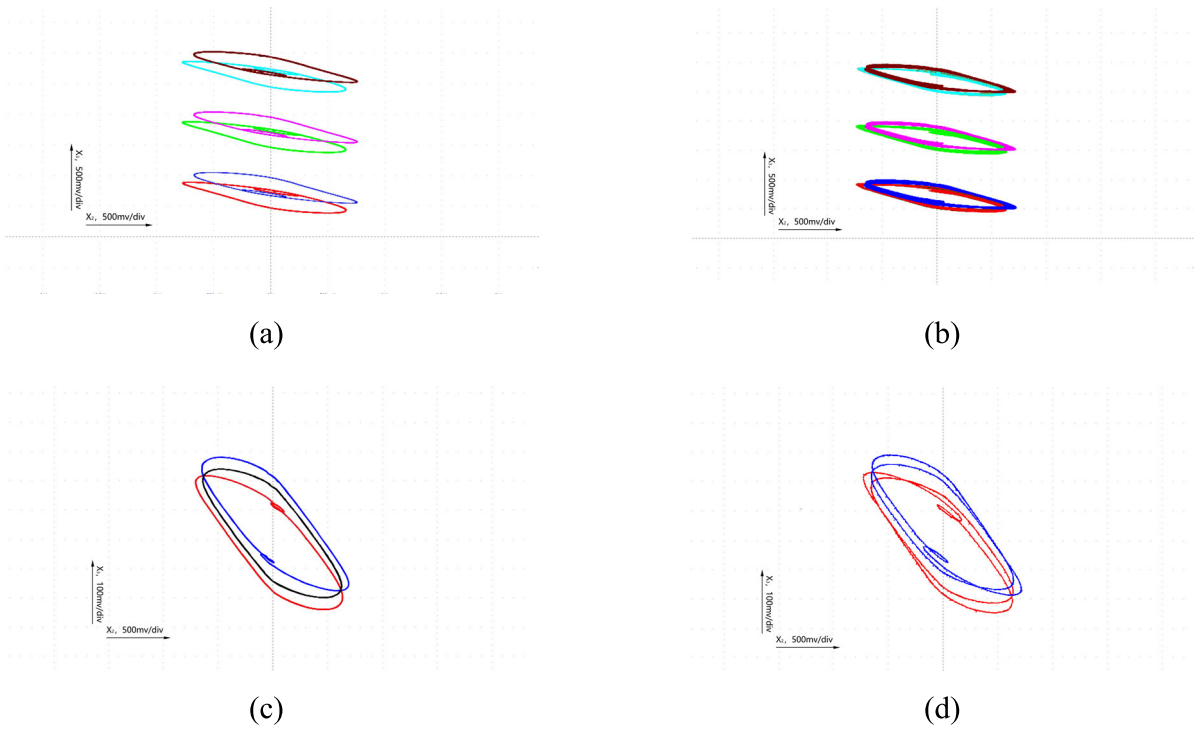

Fig. 17 Experimental results captured by the digital oscilloscope in the $x_2 - x_3$ plane: **a** period-1 attractors, **b** chaotic attractors, **c** unstable period-1 orbits, **d** unstable perido-2 orbits

of multistability. In this section, an FPGA-based digital hardware platform is developed to facilitate the physical implementation of the model and to validate the numerical simulation results.

The initial step involves discretizing the differential equations using the second-order Runge–Kutta algorithm. This discretization process is implemented on a Xilinx XC6SLX45 FPGA development board with a time step of T = 0.001, and the specific programming framework is depicted in Fig. 15. The top module is designed to ensure the orderly and error-free execution of the program, leveraging the FPGA's integrated IP cores for addition, multiplication, and floating-point operations. As a non-autonomous system, the discretization equations of the HNN incorporate an applied excitation in the form of a sinusoidal trigonometric function. Due to the FPGA's limitations in directly programming trigonometric functions, a RAM core is developed to store the precomputed values of the sinusoidal function for retrieval during execution. Additionally, the system requires the $\tanh(\cdot)$ and $\cos(\cdot)$ functions, for which no pre-existing IP cores are available within the FPGA. As a result, the $\tanh(\cdot)$ function is implemented using a piecewise linear fitting approach. Both $\tanh(\cdot)$ and $\cos(\cdot)$ are segmented into sufficiently small intervals, with each interval represented by $f(x_n) = K_n x_n + B_n$, where K_n and B_n are stored in the high and low 32 bits of a register, respectively, and are addressed based on the corresponding values of $x_i (i = 1, 2, 3)$. These transformations facilitate the development of a discrete-time model for the system, with further adjustments and scaling applied to optimize the conversion range for the digital-to-analog converter. The Verilog hardware language program generates digital signals, which are then converted into analog voltages using a dual-channel AN9767 converter and displayed on an oscilloscope (see Fig. 16).

By choosing identical parameters and initial values to those used in the numerical simulation results depicted in Fig. 9, the coexisting attractors and unstable orbits are given in Fig. 17. In Fig. 17a and b, the scale is 500 mv/div in the both x_2 and x_3 direction. In Fig. 17c and d, the scale is 500 mv/div in the x_2 direction and 100 mv/div in the x_3 direction. It is not difficult to find that the different periodic phase trajectories obtained by the FPGA are highly consistent with the image trajectories obtained from numerical simulations through observation.

6 Conclusion

In this study, the extreme multistability behavior of a two-neuron-based non-autonomous MHNN system is investigated using a semi-analytical approach, with the results further verified through numerical methods. As the strength of self-coupling between the memristor and the neuron varies, membrane potential exhibit significant complex coexisting bifurcation routes, including P-1 to P-8 motion and independent P-5 orbit. The stability of periodic motions and the classification of bifurcation points are determined based on the corresponding eigenvalues. The SN and PD bifurcations observed in the bifurcation tree play critical roles in the transitions between stable and unstable motions. Moreover, an infinite number of attractors, unstable periodic orbits, and spiking firing activities are revealed through phase diagrams and time sequence analyses, demonstrating a high degree of consistency between numerical simulations and analytical findings. Additionally, effective control over attractors is achieved by employing a rotational control strategy. Finally, the numerical and theoretical analyses are successfully validated through implementation on an FPGA platform. The primary contribution of this work lies in offering a novel perspective for comprehending the complex dynamical behavior of the system. Finally, this study provides preliminary insights into the extreme multistable behavior of the MHNN. To explore richer dynamic behaviors, future research could extend to more complex neural network architectures, such as ring networks and star networks. Furthermore, the application of rotational control strategies requires further verification, especially in high-dimensional systems. Future work could also consider introducing multi-parameter control and adaptive control methods to enhance flexibility and stability for practical applications.

Author contributions Jiakai Lu: conceptualization, formal analysis, writing-original draft, software. Fuhong Min: funding acquisition, formal analysis, supervision, writing-review & editing. Linghu Gan: investigation, visualization. Wei Zhu: methodology.

Funding This work was supported by grants from the National Natural Science Foundation of China under Grant Nos. 61971228 and 62471237, the Natural Science Foundation of Jiangsu Province, China under Bk20241880, and the

Graduate Research and Practice Innovation Program Project of Jiangsu Province under Grant No. SJCX24_0659.

Data availability No datasets were generated or analysed during the current study.

Declarations

Conflict of interest The authors declare no competing interests.

References

1. McCulloch, W.S., Pitts, W.: A logical calculus of the ideas immanent in nervous activity. Bull. Math. Biol. **5**(4), 115–133 (1943)
2. Nag Chowdhury, S., Anwar, M.S., Ghosh, D.: Cluster formation due to repulsive spanning trees in attractively coupled networks. Phys. Rev. E (2024). https://doi.org/10.1103/PhysRevE.109.044314
3. Chowdhury, S.N., Sarbendu Rakshit, C., Hens Ghosh, D.: Interlayer antisynchronization in degree-biased duplex networks. Phys. Rev. E (2023). https://doi.org/10.1103/PhysRevE.107.034313
4. Hopfield, J.J.: Neurons with graded response have collective computational properties like those of two-state neurons. Proc. Natl. Acad. Sci. **81**(10), 3088–3092 (1984)
5. Lin, H., Wang, C., Tan, Y.: Hidden extreme multistability with hyperchaos and transient chaos in a Hopfield neural network affected by electromagnetic radiation. Nonlinear Dyn. **99**(3), 2369–2386 (2019)
6. Lin, H., Wang, C., Zhang, H., Tan, Y.: Neural bursting and synchronization emulated by neural networks and circuits. IEEE Trans. Circuits Syst. I-Regul. Pap. **68**(8), 3397–3410 (2021)
7. Yu, F., Lin, Y., Yao, W., Cai, S., Lin, H., Li, Y.: Multiscroll hopfield neural network with extreme multistability and its application in video encryption for IIoT. Neural Netw. **182**, 106904 (2025)
8. Chua, L.: Memristor—the missing circuit element. IEEE Trans. Circuit Theory **18**(5), 507–519 (1971)
9. Sah, M.P., Yang, C., Kim, H., Muthuswamy, B., Jevtic, J., Chua, L.: A generic model of memristors with parasitic components. IEEE Trans. Circuits Syst. I-Regul. Pap. **62**(3), 891–898 (2015)
10. Ahmadi, A., Sriram, S., Ali, A.M., Rajagopal, K., Pal, N., Jafari, S.: A Nonlinear megastable system with diamond-shaped oscillators. Int. J. Bifurcation Chaos (2024). https://doi.org/10.1142/S0218127424500536
11. Ahmadi, A., Vijayan, V., Natiq, H., Pchelintsev, A.N., Rajagopal, K., Jafari, S.: A novel megastable chaotic system with hidden Attractors and its parameter estimation using the sparrow search algorithm. Computation **12**(12), 245 (2024)
12. Lu, Y., Wei, X., Huang, X., Yin, Z.: Memristive characteristics and extreme multistability of LLC DC-DC resonant converters. IEEE Trans. Ind. Electron. **71**(7), 7020–7029 (2024)
13. Li, Y., Li, C., Lei, T., Yang, Y., Chen, G.: Offset boosting-entangled complex dynamics in the memristive Rulkov neuron. IEEE Trans. Ind. Electron. **71**(8), 1–11 (2024)
14. Wan, Q., Yan, Z., Li, F., Liu, J., Chen, S.: Multistable dynamics in a Hopfield neural network under electromagnetic radiation and dual bias currents. Nonlinear Dyn. **109**(3), 2085–2101 (2022)
15. Boui, F., Kengne, J., Djuidje Kenmoe, G., Effa, J.Y.: Four-scroll attractor on the dynamics of a novel Hopfield neural network based on bi-neurons without bias current. Heliyon **8**(10), e11046 (2022)
16. Foss, J., Longtin, A., Mensour, B., Milton, J.: Multistability and delayed recurrent loops. Phys. Rev. Lett. **76**(4), 708–711 (1996)
17. Doubla, I.S., Njitacke, Z.T., Ekonde, S., Tsafack, N., De, J., Kengne, J.: Multistability and circuit implementation of tabu learning two-neuron model: application to secure biomedical images in IoMT. Neural Comput. Appl. **33**(21), 14945–14973 (2021)
18. Chowdhury, S.N., Ghosh, D.: Hidden attractors: a new chaotic system without equilibria. Eur. Phys. J.-Spec. Top. **229**(6–7), 1299–1308 (2020)
19. Cui, W., Jiao, S., Gao, R., Li, Y., Liu, H.: A single-parameter multi-stable stochastic resonant nonlinear system with external signal coupled control and its application. Measurement **243**, 116280 (2025)
20. Shen, Y., Li, Y., Li, W., Yao, Q., Gao, H.: Extremely multistable grid-scroll memristive chaotic system with omni-directional extended attractors and application of weak signal detection. Chaos Solitons Fractals **190**, 115791–115791 (2024)
21. Pati, N., Garai, S., Hossain, M., Layek, G.C., Pal, N.R.: Fear induced multistability in a predator-prey model. Int. J. Bifurcation Chaos **31**(10), 2150150–2150150 (2021)
22. Pati, N.C., Rech, P.C., Layek, G.C.: Multistability for nonlinear acoustic-gravity waves in a rotating atmosphere. Chaos (2021). https://doi.org/10.1063/5.0020319
23. Hens, C., Dana, S.K., Feudel, U.: Extreme multistability: attractor manipulation and robustness. Chaos (2015). https://doi.org/10.1063/1.4921351
24. Deb, P., Layek, G.C.: Controlling the period-bubbling route to chaos. Int. J. Bifurcation Chaos (2024). https://doi.org/10.1142/S0218127424501232
25. Liu, J., et al.: A chameleon system with a cosine function: bifurcation analysis, multistability, and offset boosting. Phys. Scr. (2025). https://doi.org/10.1088/1402-4896/adb342
26. Badri, V., Tavazoei, M.S.: Achievable performance region for a fractional-order proportional and derivative motion controller. IEEE Trans. Ind. Electron. **62**(11), 7171–7180 (2015)
27. Dai, L., Li, X., Zhu, Y., Zhang, M.: Enhancing settling performance of precision motion systems by phase-based variable gain feedback control. IEEE Trans. Ind. Electron. **68**(5), 4099–4108 (2020)
28. Ma, J., Wu, F., Jin, W., Zhou, P., Hayat, T.: Calculation of Hamilton energy and control of dynamical systems with different types of attractors. Chaos (2017). https://doi.org/10.1063/1.4983469
29. Zhang, S., Zheng, J., Wang, X., Zeng, Z., He, S.: Initial offset boosting coexisting attractors in memristive multi-

double-scroll Hopfield neural network. Nonlinear Dyn. **102**(4), 2821–2841 (2020)
30. Bao, H., Chen, Z., Chen, M., Xu, Q., Bao, B.: Memristive-cyclic Hopfield neural network: spatial multi-scroll chaotic attractors and spatial initial-offset coexisting behaviors. Nonlinear Dyn. **111**(24), 22535–22550 (2023)
31. Korkmaz, N.: A phase control method for the dynamical attractor of the HR neuron model: the rotation-transition process and its experimental realization. Neural. Process. Lett. **53**(6), 3877–3892 (2021)
32. Luo, A.C.J.: Periodic flows to chaos based on discrete implicit mappings of continuous nonlinear systems. Int. J. Bifurc. Chaos **25**(3), 1550044 (2015)
33. Min, F., Xue, L.: Routes toward chaos in a memristor-based Shinriki circuit. Chaos (2023). https://doi.org/10.1063/5.0126900
34. Min, F., Zhu, J., Cheng, Y., Xu, Y.: Dynamical analysis of a tabu learning neuron through the discrete implicit mapping method. Chaos Solitons Fractals **181**, 114716 (2024)
35. Xu, Q., Song, Z., Bao, H., Chen, M., Bao, B.: Two-neuron-based non-autonomous memristive Hopfield neural network: Numerical analyses and hardware experiments. AEU-Int. J. Electron. Commun. **96**, 66–74 (2018)
36. Chen, C., Min, F., Zhang, Y., Bao, H.: Relu-type Hopfield neural network with analog hardware implementation. Chaos Solitons Fractals (2022). https://doi.org/10.2139/ssrn.4285384
37. Doubla, I.S., Ramakrishnan, B., Njitacke, Z.T., Kengne, J., Rajagopal, K.: Hidden extreme multistability and its control with selection of a desired attractor in a non-autonomous Hopfield neuron. AEU-Int. J. Electron. Commun. **144**, 154059 (2022)
38. Bao, H., Hua, M., Ma, J., Chen, M., Bao, B.: Offset-control plane coexisting behaviors in two-memristor-based Hopfield neural network. IEEE Trans. Ind. Electron. **70**(10), 10526–10535 (2022)
39. Xu, B., Luo, X., Wang, Y., Bai, L., Chen, K., Zhao, J.: A 4D trigonometric-based memristor hyperchaotic map to ultra-fast PRNG. IEEE Trans. Ind. Informat. **20**(6), 8673–8683 (2024)
40. Sun, J., Li, C., Wang, Z., Wang, Y.: A memristive fully connect neural network and application of medical image encryption based on central diffusion algorithm. IEEE Trans. Ind. Informat. **20**(3), 3778–3788 (2023)
41. Sun, J., Yang, J., Liu, P., Wang, Y.: Design of general flux-controlled and charge-controlled memristor emulators based on hyperbolic functions. IEEE Trans. Comput.-Aided Design Integr. Circuits. Syst. **42**(3), 956–967 (2023)
42. Ma, X., Li, C., Li, Y., Bi, L., Qi, Z.: Rotation control of an HR neuron with a locally active memristor. Eur. Phys. J. Plus (2022). https://doi.org/10.1140/epjp/s13360-022-02761-0
43. Li, Y., Liu, J., Liu, H.: A complex-variable disturbed laser with application to hidden multi-scroll attractor generation. Nonlinear Dyn. (2024). https://doi.org/10.1007/s11071-024-10598-8
44. Huang, K., Li, C., Zhang, X., Moroz, I., Liu, Z.: Constructing a memristive chaotic oscillator with two-dimensional offset boosting. IEEE Trans. Comput.-Aided Design Integr. Circuits Syst. (2024). https://doi.org/10.1109/TCAD.2024.3434478
45. Waldner, F., Klages, R.: Symmetric Jacobian for local Lyapunov exponents and Lyapunov stability analysis revisited. Chaos Solitons Fractals **45**(3), 325–340 (2012)

Publisher's Note Springer Nature remains neutral with regard to jurisdictional claims in published maps and institutional affiliations.

Springer Nature or its licensor (e.g. a society or other partner) holds exclusive rights to this article under a publishing agreement with the author(s) or other rightsholder(s); author self-archiving of the accepted manuscript version of this article is solely governed by the terms of such publishing agreement and applicable law.